Title

Zinc-copper dual-ion electrolytes to suppress dendritic growth and increase anode utilization in zinc ion capacitors

Journal

Science Advances, 10(1)

ISSN

2375-2548

Authors

Shin, Chanho

Yao, Lulu

Jeong, Seong-Yong

et al.

Publication Date

2024-01-05

DOI

10.1126/sciadv.adf9951

ELECTROCHEMISTRY

Zinc-copper dual-ion electrolytes to suppress dendritic growth and increase anode utilization in zinc ion capacitors

Chanho Shin[1], Lulu Yao[1], Seong-Yong Jeong[2,3], Tse Nga Ng[1,4]*

The main bottlenecks that hinder the performance of rechargeable zinc electrochemical cells are their limited cycle lifetime and energy density. To overcome these limitations, this work studied the mechanism of a dual-ion Zn-Cu electrolyte to suppress dendritic formation and extend the device cycle life while concurrently enhancing the utilization ratio of zinc and thereby increasing the energy density of zinc ion capacitors (ZICs). The ZICs achieved a best-in-class energy density of 41 watt hour per kilogram with a negative-to-positive (n/p) electrode capacity ratio of 3.10. At the n/p ratio of 5.93, the device showed a remarkable cycle life of 22,000 full charge-discharge cycles, which was equivalent to 557 hours of discharge. The cumulative capacity reached ~581 ampere hour per gram, surpassing the benchmarks of lithium and sodium ion capacitors and highlighting the promise of the dual-ion electrolyte for delivering high-performance, low-maintenance electrochemical energy supplies.

INTRODUCTION

Metal ion capacitors are hybrid electrochemical cells that bridge the divide between batteries and electrochemical capacitors, enabling them to provide high energy densities at rapid charging or discharging rates. These devices combine a redox metal anode, similar to that found in batteries, to enhance the capacity for charge storage and an electric double-layer cathode that allows fast kinetics and sustains high power density. The first metal ion capacitors were based on lithium (*1*) and sodium ions (*2*–*4*), but potential safety hazards associated with these metals prompted the search for other alternatives (*5*). In particular, zinc ion capacitors (ZICs) emerge as an appealing choice with advantages of environmental safety, a high theoretical capacity of 820 mAh/g as a divalent system, and an abundance of zinc reserves unaffected by geopolitical factors (*6*–*8*). However, zinc ion devices have been limited by instability upon redox cycling and low utilization of the anode, which substantially reduce the specific energy of the devices and hinder their commercial viability (*9*–*13*).

The challenges with cycling stability and low utilization of the anode are intertwined; as the amount of accessible zinc is depleted with cycling degradation, prior works compensated for it by using thick foils. This approach led to only a small fraction of the zinc being cycled, i.e., operating at low utilization, typically below a few percent (*11*). The excessive capacity of the anode creates a large imbalance in electrode utilization and results in poor energy density in a full cell, rendering it impractical for commercialization. Therefore, it is crucial to eliminate the cause of cycling loss to enable high utilization, ideally to achieve a balanced n/p ratio of 1, and achieve competitive metrics, targeting >40 Wh/kg and more than 2000 redox cycles (*9*, *11*).

The dominant degradation mechanism involves the formation of zinc dendrites during plating and stripping processes on the anode. Grain growth along (101) and (100) planes of the hexagonal closed pack structure of zinc tends to be randomly oriented (*14*, *15*). Upon redox cycling, the electric field concentration on the tips of grains would accelerate the deposition of zinc ions and lead to dendritic protrusions that can break off or even pierce the separator and cause catastrophic short circuits. To mitigate dendritic problems, researchers have added electrolyte additives (*16*–*21*) or ion distributors (*22*–*26*) to redirect zinc concentration for more uniform deposition, but these two methods slowed down the redox kinetics and consequently reduced the power densities. A third method that avoided the trade-off with kinetics involved promoting zinc deposition on its (002) plane to favor a planar orientation (*27*–*30*). For example, it was shown that Cu (100) substrates (*14*) would enhance planar grain growth and that CuZn alloys (*10*, *31*) suppress dendrites due to its low surface energy for zinc ions to bind evenly over the surface. While these surface modifications initially reduce dendrite formation close to the substrate, the effectiveness of the CuZn layer would diminish as thicker layers of zinc are plated. Thus, the anode loading is limited to a low areal capacity; otherwise, dendrite formation would resume and shorten the cycle life.

To suppress dendrites and enable high loading and utilization, our strategy is to design a zinc-copper dual-ion electrolyte for use with zinc anodes as shown in Fig. 1. The incorporation of copper ions in the electrolyte facilitates CuZn alloy deposition during the anode plating/stripping processes. In contrast to previous methods where alloys on the substrate surface would be screened by newly deposited zinc, here, the CuZn is replenished from the electrolyte to maintain the preference for planar grain growth. The potential use of copper ions in electrolytes might have been previously overlooked because of detrimental copper oxide formation in aqueous electrolyte; here, we chose nonaqueous solvents (*32*, *33*) to circumvent the oxide problem. The plating/stripping overpotentials are analyzed to reveal the mechanism for preventing dendrites at the anode. Using the dual-ion electrolyte, ZICs consisting of activated carbon at the cathode and electroplated zinc at the anode were operated for 22,000 redox cycles (equivalent to 557 hours) to evaluate the cell stability and determine the cumulative capacity before cell shorting. The ZICs were fabricated with high areal capacities of 0.74 mAh/cm^2

[1]Program in Materials Science and Engineering, University of California San Diego, 9500 Gilman Drive, La Jolla, CA 92093, USA. [2]Department of Nanoengineering, University of California San Diego, 9500 Gilman Drive, La Jolla, CA 92093, USA. [3]Division of Advanced Materials Engineering, Kongju National University, Chungnam, 31080, Republic of Korea. [4]Department of Electrical and Computer Engineering, University of California San Diego, 9500 Gilman Drive, La Jolla, CA 92093, USA.
*Corresponding author. Email: tnn046@ucsd.edu

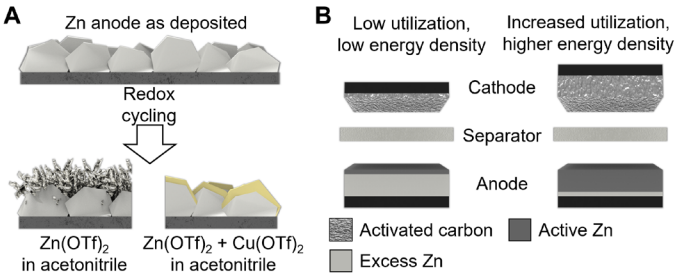

Fig. 1. Issues of dendrites and low utilization at the anode in zinc ion devices. (**A**) Concept of using a dual-ion electrolyte to suppress dendrite formation. (**B**) Minimizing excess zinc capacity by plating and stripping a higher portion of the anode to increase areal energy densities.

and better balanced n/p ratios to showcase their performance under practical conditions and to allow for comparisons with state-of-the-art metal ion capacitors.

RESULTS AND DISCUSSIONS

Evolution of the anode composition and surface morphology with redox cycling

Figure 2 presents the changes in morphology and composition observed at the anode, following galvanostatic charge-discharge (GCD) of the ZICs between 0 and 2 V at a current density of 25 mA/cm^2. The ZICs were coin cells prepared according to the descriptions in Methods, and, after GCD cycling, the cells were disassembled to image the anodes. Before any redox cycle, the as-fabricated zinc anode showed an average surface roughness (S_a) of 1.3 μm, with several protruded features more than 15 μm tall in the area scanned by the three-dimensional (3D) optical profiler. For the cell with 0.5 M zinc triflate electrolyte, the anode roughness increased to 2.3 μm after 1600 cycles, and the cell was short circuited because of some zinc dendrites piercing through the separator. Meanwhile, for the cell with the dual-ion Zn-Cu electrolyte [0.5 M zinc triflate $Zn(OTf)_2$ and 0.1 M copper triflate $Cu(OTf)_2$], the anode maintained a roughness comparable to the initial surface in Fig. 2A after undergoing 1600 cycles. With the Zn-Cu electrolyte, the cell continued to function even after 10,000 cycles, with a roughness of 2.0 μm as depicted in fig. S1.

Figure 2B shows the x-ray diffraction patterns of the anodes after GCD cycling in either the Zn-only or Zn-Cu electrolyte. The as-fabricated zinc film showed a dominant peak at 43.2° representing the Zn(101) crystal orientation. For the anode after 1000 cycles in the Zn-only electrolyte, the diffraction pattern remained similar to the initial measurement. Whereas after 1000 cycles in the Zn-Cu electrolyte, the anode showed a slight increase in the peak at 36.3°, indicating crystal growth in the Zn(002) orientation, which would favor planar grain deposition (*14*) as illustrated in Fig. 2C. As GCD proceeded to 5000 cycles, a peak at 41.8° emerged and corresponded to the incorporation of $CuZn_5$ alloy in the anode. Subsequently at 10,000 cycles, the $CuZn_5$ peak surpassed the intensity of the Zn(101) peak, showing the substantial involvement of the alloy in long-term cycling processes.

The scanning electron microscopy (SEM) images in Fig. 2 (D to G) compared the anode surface morphologies and showed the extent of dendrite formation in Zn-only and Zn-Cu electrolytes. After 1000 GCD cycles in the Zn-only electrolyte, the anode in Fig. 2E was covered

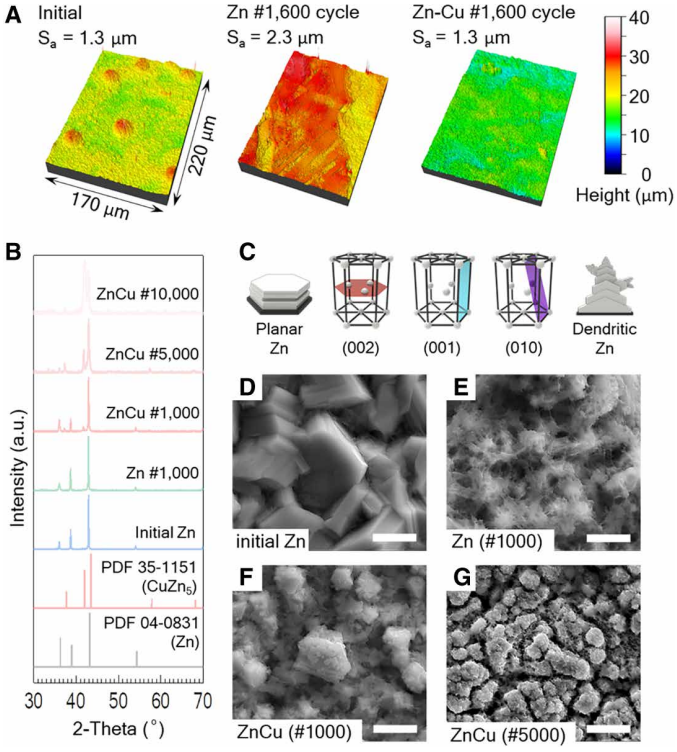

Fig. 2. Surface roughness and composition analyses. All cycles were carried out on full cells at a current density of 25 mA/cm^2. (**A**) Surface morphologies of Zn anodes after 1600 redox cycles in either Zn or Zn-Cu electrolyte. (**B**) X-ray diffraction patterns of anodes as a function of redox cycles and electrolytes. The reference powder diffraction files (PDF) are included for Zn and $ZnCu_5$. (**C**) Various crystallographic orientations of Zn. (**D** to **G**) SEM images of anode surfaces after cycling in different electrolytes. Scale bars, 2 μm.

by dendrites, and the initially large grains were stripped away. The anode cycled in Zn-Cu electrolyte showed that the stripping and plating process introduced submillimeter-scale roughness, but the granular structures were retained after 1000 GCD cycles, as seen in Fig. 2F. The CuZn alloy was detected in the anode, as evident from the weight percent of copper (11%) to zinc (89%) measured by energy dispersive x-ray spectroscopy in fig. S2. After 5000 cycles, the grain sizes were further reduced, but dendrites were not prevalent in Fig. 2G. By 10,000 cycles, the depletion of Cu ion in the anode was observed, where the percentage of Cu was only 0.5 wt % (fig. S2). Because of the Cu depletion in the electrolyte, the suppression of dendrite formation became ineffective. However, because of the underlying CuZn alloy, the growth of dendrites was isotropic and less inclined to develop only vertically toward the separator, as in the case of Fig. 2E. Consequently, the ZIC with the Zn-Cu electrolyte was not short circuited by the 10,000 cycles and continued to work up to 22,000 cycles with the anode at the n/p ratio of 5.93.

Since the ZICs were pseudocapacitive, the device current was influenced by both capacitive and diffusion-controlled factors. To separate the capacitive and diffusion-controlled contributions, we used the relation (*34*–*37*) $i/\nu^{0.5} = k_1 \nu^{0.5} + k_2$, where k_1 is the capacitive-controlled constant, k_2 is the diffusion-controlled constant, i is the current, and ν is the scan rate. This relation was fitted to the total current; an example is shown in the inset of fig. S3A. For

the ZICs in this work, fig. S3 (B and C) shows that the contribution from capacitive current was at least four times higher than the diffusion-controlled current, indicating that the charge storage mechanism was dominantly capacitive and would support fast kinetics and high-power output.

Mechanisms of nucleation and growth in Zn versus Zn-Cu electrolyte

The zinc nucleation and grain growth mechanisms (*38*–*41*) in the two electrolytes were revealed by examining the changes of the anode potential during the plating and stripping processes with respect to the reference electrode of Zn/Zn^{2+}. The examples in Fig. 3A showed that an overpotential up to −0.2 V was needed for zinc plating at a current density of 25 mA/cm^2. In the Zn-only electrolyte, there was a rapid jump of potential from −0.1 to −0.2 V as the current was applied, and then the potential change was relatively small, below 20 mV over a period of 25 s. The abrupt initial increase in potential was linked to the nucleation step of forming zinc clusters. The subsequent change in potential was referred to as the plateau overpotential (*38*) associated with the growth of already existing nuclei. Since the plateau overpotential was small relative to that of nucleation, this observation indicated that addition of zinc to preexisting nuclei was more favorable and had a lower energy barrier than forming new clusters.

In the Zn-Cu electrolyte, upon applying the deposition current, the anode potential was initially at 0.2 V and dropped to −0.03 V within the first 5 s. This change was attributed to the process of reducing copper ions. As the deposition progressed, the potential gradually shifted from −0.03 to −0.115 V, resulting in a plateau overpotential of ~75 mV. The relatively large shift in potential suggested that additional zinc plating in the Zn-Cu electrolyte involved both nucleation and growth and that the preference for zinc growth over nucleation was not as pronounced as in Zn-only electrolyte.

The radius of electrodeposited zinc clusters can be estimated by using the Gibbs free energy equation for nucleation (*38*): $\Delta G_{nucleation} = -(4/3)\pi r^3 \Delta G_V + 4\pi r^2 \Upsilon$, where r is the radius of spherical nuclei, ΔG_V is the free energy change per volume, and Υ is the surface energy between the electrolyte and the anode. The radius of a cluster is assumed to be at an equilibrium point when the bulk free energy ($-4/3\ \pi r^3 \Delta G_V$) equals to the surface free energy ($4\pi r^2 \Upsilon$), that is, when $\Delta G_{nucleation} = 0$. The deposition overpotential η is related to ΔG_V by $= F|\eta|/V_m$, where F is the Faraday's constant and V_m is the molar volume (*42*) of zinc ($V_m = 9.157 \times 10^{-6}$ m^3/mol). Solving for the cluster radius r when $\Delta G_{nucleation} = 0$, the expression becomes

$$r = \frac{3\Upsilon}{\Delta G_V} = \frac{3\Upsilon V_m}{F|\eta|} \quad (1)$$

The expression demonstrates the inverse correlation between the cluster radius and the overpotential. As shown in Fig. 3B, the plateau overpotential of the anode in the Zn-Cu electrolyte was higher than in the Zn-only electrolyte, while the surface energy was slightly lower in the Zn-Cu system (measurements provided in the Supplementary note). From the calculations included in Supplementary note based on fig. S4, the cluster radius was estimated to be 1.63 nm in the Zn-Cu electrolyte and 12.1 nm in the Zn-only electrolyte. The smaller cluster radius in the Zn-Cu electrolyte facilitated more uniform, planar coverage compared to the large nuclei that led to vertical dendritic growth as shown in Fig. 3F.

To check the reversibility of zinc anode in each electrolyte, Zn/Zn symmetric cells in Fig. 3C were tested and shown to reach the cutoff capacity of 0.42 and 0.84 mAh/cm^2. The higher cutoff capacity was achieved by increasing the Cu concentration from 0.1 to 0.2 M in the Zn-Cu electrolyte. In Fig. 3 (D and E), the cells with Zn-only electrolyte were short circuited after 36 and 62 hours. Meanwhile, the symmetric cells with Zn-Cu electrolyte remained functional for 90 hours, and the overpotential shifted only after ~1000 cycles. Thus, the Zn-Cu electrolyte facilitated better cycling stability compared to Zn-only electrolyte across different cutoff capacities.

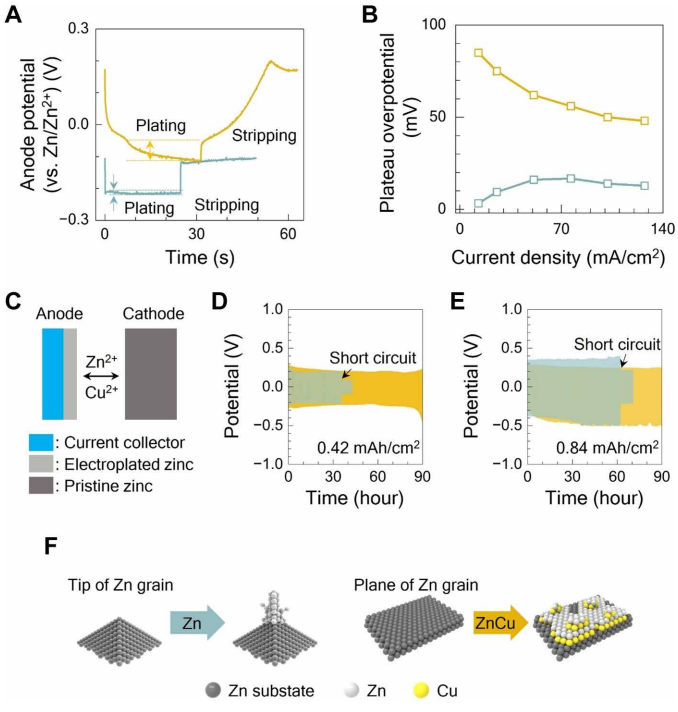

Fig. 3. Effects of electrolytes on anode potential. Blue, Zn-only electrolyte; orange, Zn-Cu electrolyte. (**A**) Anode potential change measured with a three-electrode configuration at a current density of 25 mA/cm^2. The plateau overpotentials are labeled by the arrows. (**B**) The plateau overpotentials of Zn anodes in Zn-Cu and Zn-only electrolytes as a function of charging current densities. (**C**) Device structure of Zn/Zn symmetric cell. Potential change with cycling at a current density of 25 mA/cm^2 of Zn/Zn symmetric cells with a cutoff capacity of (**D**) 0.42 and (**E**) 0.84 mAh/cm^2 in the Zn-Cu electrolyte. The cells shorted in Zn electrolyte but continued cycling in Zn-Cu electrolyte. (**F**) Schematics of grain growth mechanisms of Zn and CuZn on the anode surface.

Performance comparisons of ZICs with Zn versus Zn-Cu electrolyte

Figure 4 displays the characteristics of ZICs using the Zn-only (blue curves) and the Zn-Cu (orange curves) electrolytes. The cyclic voltammetry current-voltage characteristics of the Zn-Cu device exhibited a more square shape compared to that of the Zn-only device, resulting in 14% higher capacitance of 1.6 F for Zn-Cu and 1.4 F for Zn-only, from Fig. 4 (A and C), respectively. In Fig. 4 (B and D), the GCD data at current densities ≥22.5 mA/cm^2 showed longer

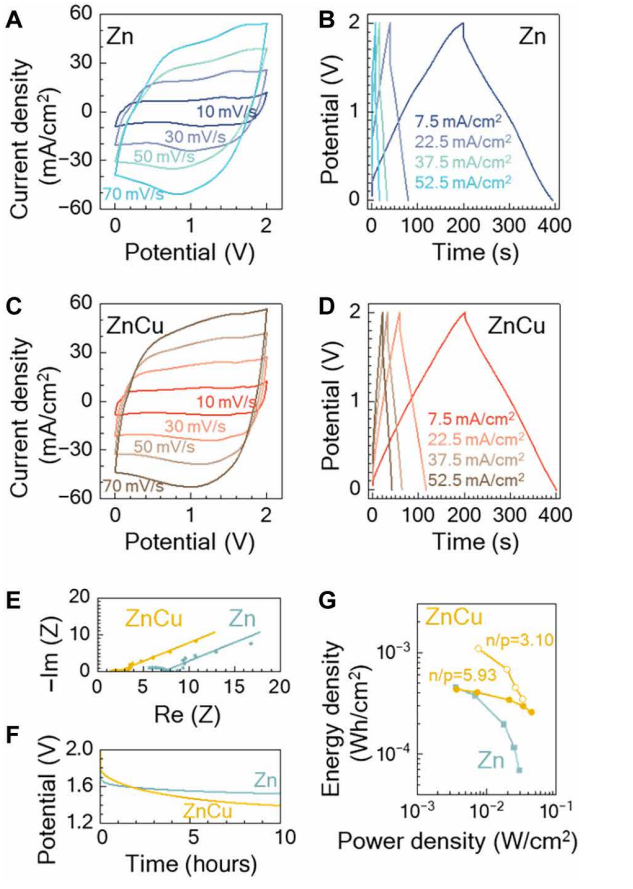

Fig. 4. Performance comparison of ZICs with different electrolytes. Cyclic voltammetry was measured at scan rates of 10 to 70 mV/s with (**A**) Zn and (**C**) Zn-Cu electrolytes. GCD measurements were taken at current densities of 7.5 to 52.5 mA/cm^2 with (**B**) Zn and (**D**) Zn-Cu electrolytes. (**E**) Nyquist plots of capacitors in different electrolytes in the frequency range of 0.01 Hz to 100 kHz. (**F**) After being charged to 2 V and set to the open-circuit state, the potential decay of two cells with different electrolytes. (**G**) Energy densities versus power densities of the capacitors with the Zn or Zn-Cu electrolyte.

discharging times and therefore higher capacities for the Zn-Cu capacitor than the Zn-only device. At a current density of 7.5 mA/cm^2, while both types of capacitors showed similar discharging times, the Zn-Cu capacitor displayed a smaller voltage drop at the start of discharge. This observation was further supported by electrochemical impedance measurements in Fig. 4E, where the equivalent series resistance (ESR) was three times lower in the Zn-Cu cell than Zn alone.

The self-discharge (*43*) characteristics in Fig. 4F were measured after the capacitors were charged to 2 V, and the open-circuit voltage was sampled once every 0.1 s. Since the electrodes were made with the same materials and loading, the differences in self-discharge were attributed to the influence of electrolytes. The voltage decay was slightly worse in the Zn-Cu device with 0.6 V drop, in contrast to the 0.5 V drop in the Zn-only device after 10 hours. The reason for higher self-discharge in Zn-Cu electrolyte was due to the spontaneous reaction between zinc and copper ions. As copper ions have a higher standard cell potential (E^0 of $Cu^{2+}+2e^- \rightarrow Cu$ is 0.34 V) compared to zinc (E^0 of $Zn^{2+} + 2e^- \rightarrow Zn$ is −0.76 V), the reduction of copper ions by oxidizing zinc occurred spontaneously. Consequently, a portion of the zinc electrode was stripped away and manifested as the voltage decay. Nonetheless, the reaction between copper ions and the zinc electrode did reach equilibrium after 10 hours because the increased Cu concentration on the anode surface changed the surface redox potential, stabilizing the anode and preventing further electrolyte reaction as seen in the cell voltage plateau in Fig. 4F.

The areal energy and power densities of the Zn-Cu and Zn-only capacitors are summarized in Fig. 4G. The cells showed similar energy densities at low power < 0.02 W/cm^2, but for high-power charging/discharging, the Zn-Cu cell with its improved ESR maintained the energy densities better than the Zn-only cell.

The loading of active materials at the cathode and the anode should be matched in their capacities to avoid unused materials and maximize the energy density. However, with ZICs, the anode typically contained excess capacity compared to the cathode. In this work, we mitigated this imbalance and decreased the n/p ratios to 3.10 by increasing the loading of activated carbon per unit area at the cathode. The calculations of n/p ratio and cumulative capacity are defined in Methods. The ideal n/p ratio is 1 to maximize cathode and anode balance. As shown in Fig. 4G at the power density of 22 mW/cm^2, the energy density was improved to 0.74 mWh/cm^2 at the n/p ratio of 3.10, compared to 0.34 mWh/cm^2 at the n/p ratio of 5.93. The areal capacity was doubled by improving the n/p ratio.

Comparison of metal ion capacitors on stability and cumulative capacity

While the smaller n/p ratio enhanced the energy densities, it was observed to trade-off with redox cycling stability. Figure 5A presents the capacity retention of the devices as a function of the n/p ratio. For the capacitor at the n/p ratio of 5.93, the Zn-Cu electrolyte had suppressed dendritic formation and allowed the cell to retain 90% of its original capacity after 25,000 GCD cycles. However, at the n/p ratio of 3.10, the cell retention dropped below 90% by 6700 cycles. This degradation with decreasing n/p ratio was partially caused by the depletion of copper ions in the electrolyte, leading to the reappearance of dendrites, which caused short circuits.

Figure 5B demonstrates that the cycle life and cumulative capacity of Zn-Cu capacitors were improved by adjusting the copper ion concentration in electrolyte (0.1 M for the n/p ratio of 5.93 and 0.2 M for the n/p ratio of 3.10). We note that there was an optimal concentration of copper ion for different n/p ratios. With a decreasing n/p ratio, more zinc cations were dissolved into the electrolytes as the cell discharged; thus, there was an increasing concentration of Zn. To match that Zn increase as the n/p ratio decreased, the concentration of Cu ions should be increased to provide sufficient Cu for ZnCu alloy formation. However, when the copper ion concentration was increased beyond 0.2 M, the large extent of spontaneous copper reduction at the anode interfered with the zinc plating and stripping process, and, therefore, we kept the maximum copper ion concentration to be 0.2 M in the electrolyte.

The cumulative capacities of ZICs generally showed a similar tendency with n/p ratio as depicted in Fig. 5C. In prior works as listed in Table 1, the cumulative capacity of (*44*) reached up to 4.5 Ah/cm^2 due to dendrite suppression, but the anode was at very large excess with the n/p ratio = 55.6, meaning that a substantial portion of the anode remained unused and ultimately not contributing to energy storage. For a more balanced n/p ratio of 3.88 from (*10*), the reported cumulative capacity was below 3.2 Ah/cm^2 on the

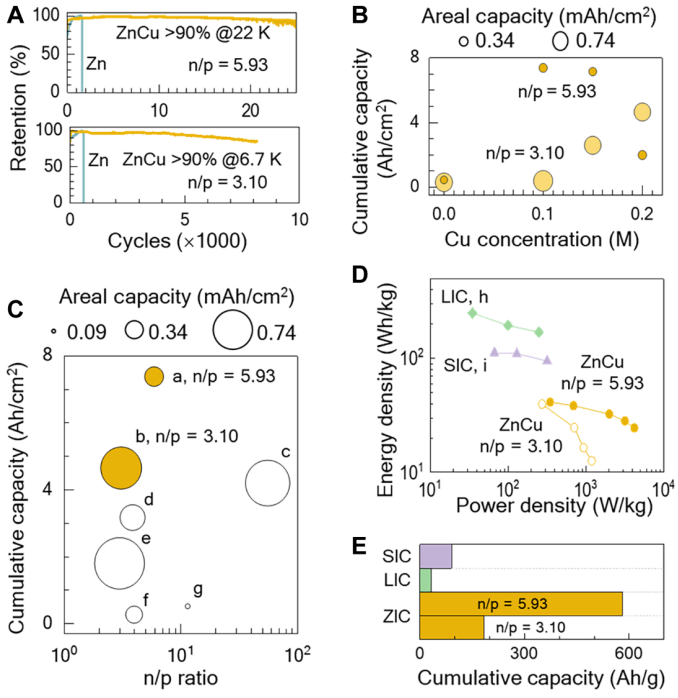

Fig. 5. Comparisons of metal ion capacitors on cycling stability and cumulative capacity. Redox cycling of ZICs was carried out between 0 and 2 V at a current density of 25 mA/cm^2. (**A**) Capacity retention for the Zn-only or Zn-Cu electrolyte, for cells with different n/p ratios. (**B**) Cumulative capacities as a function of copper ion concentration in the Zn-Cu electrolyte. (**C**) Cumulative capacities as a function of n/p ratios. Black circles are from state-of-the-art references as listed in Table 1. Orange circles are from the capacitors with Zn-Cu electrolyte in this work. (**D**) Gravimetric energy and power densities of metal ion capacitors: lithium (LIC), sodium (SIC), and zinc with the Zn-Cu electrolyte in this work. (**E**) Gravimetric cumulative capacities of metal-ion capacitors. The references for SIC and LIC are provided in Table 1.

Table 1. Structure and metrics of metal ion capacitors. AC, activated carbon. DES, deep eutectic solvent. AN, acetonitrile. DMF, dimethylformamide. ME, methanol. NHP, ammonium dihydrogen phosphate. EC, ethylene carbonate. DEC, diethyl carbonate. DMC, dimethyl carbonate.

	Electrode (Anode||Cathode)	Electrolyte	Current density (A/g)	Areal capacity (mAh/cm^2)	n/p ratio	Cumulative capacity (Ah/cm^2)	Ref.
a	Zn||AC	0.5 M $Zn(OTf)_2$ and 0.1 M or 0.2 M $Cu(OTf)_2$ in AN	2.5	0.340	5.93	7.4	This Work*
b			1.3	0.738	3.10	4.7	
c	DES-Zn||AC	$ZnSO_4$ in H_2O	4	0.45	3.88	3.2	(*10*)
d	Zn||AC	$ZnSO_4$ in H_2O/DMF	0.5	1.00	55.6	4.2	(*44*)
e	Zn||AC	$ZnSO_4$ in H_2O/ME	2	0.9	3	1.8	(*45*)
f	Zn||AC	$ZnSO_4$ in H_2O/NHP	0.5	0.3	4	0.27	(*46*)
g	Zn||AC	$ZnSO_4$ in H_2O	4	0.087	11.5	0.5	(*26*)
h	$LiFe_3O_4$/G||Graphene	$LiPF_6$ in EC/DEC/DMC	2	205 mAh/g	-	31 Ah/g	(*47*)
i	Na-C||AC	$NaClO_4$ in EC/DEC	5	107 mAh/g	-	90 Ah/g	(*4*, *48*)

*The cumulative capacity was calculated from the sum of GCD cycles for which the Coulombic efficiency was over 99%, and the capacity retention exceeded 90%.

$CuZn_4$ alloy substrate with a lifetime of ~7000 cycles (250 hours). In this study, by replenishing the CuZn alloy with Zn-Cu electrolyte, the cumulative capacity of our devices surpassed previous state-of-the-art records and achieved 7.4 Ah/cm^2 at n/p ratio = 5.93 and 4.7 Ah/cm^2 at n/p = 3.10. The cycle lifetime was 22,000 cycles (equivalent 557 hours) and 6700 cycles (347 hours), respectively.

The gravimetric energy and power densities of our ZICs with the Zn-Cu electrolyte were compared to those of lithium and sodium

Table 2. Dimensions and materials loading of the cells measured in this work.

	Components	Dimensions	Notes
Fig. 3, A and B	• Cathode loading of activated carbon: 8.24 mg • Anode loading of Zn: 1.62 mg	Round samples with 1-cm diameter	Zn-Cu electrolyte was 0.5 M $Zn(OTf)_2$ and 0.1 M $Cu(OTf)_2$
Fig. 3, C and D	• Cathode loading of Zn: 10.9 mg • Anode loading of Zn: 2.74 mg • 160 µl electrolyte	Round samples with 1.3-cm diameter	Zn-Cu electrolyte was 0.5 M $Zn(OTf)_2$ and 0.1 M $Cu(OTf)_2$ or 0.2 M $Cu(OTf)_2$
Fig. 4	• Cathode loading of activated carbon: 14 mg • Anode loading of Zn: 2.74 mg • 160 µl electrolyte	Round samples with 1.3-cm diameter	Zn-Cu electrolyte was 0.5 M $Zn(OTf)_2$ and 0.1 M $Cu(OTf)_2$
Fig. 5	• Cathode loading of activated carbon: 14 mg (n/p = 5.93) or 34 mg (n/p = 3.10) • Anode loading of Zn: 2.74 mg • 160 µl electrolyte • Separator: 13.5 mg • Carbon cloth current collectors: 16 mg total	Round samples with 1.3-cm diameter	Calculations of gravimetric energy/power densities included the loading of activated carbon and Zn but not carbon cloth or separator.

ion capacitors in Fig. 5D. At a power density of 300 W/kg, the ZICs demonstrated an energy density of 41 Wh/kg for the cell at the n/p ratio of 5.93. This energy density was calculated on the basis of active materials, which were the sum of zinc and activated carbon. When including the weights of current collector and separator components, the energy density was 14.9 Wh/kg, still within an order of magnitude of the level practical for commercialization (>40 Wh/kg) according to (*9*, *11*). While the energy densities of ZICs were lower than their lithium and sodium counterparts, the power densities of ZICs were superior, reaching up to 3.5 kW/kg. Moreover, the cumulative capacities of ZICs were far higher than lithium and sodium ion capacitors, better by 2- to 18-fold as shown in Fig. 5E, because of the excellent cycling stability of ZICs when dendritic formation was suppressed with the appropriate choice of electrolyte.

The remarkable cumulative capacity demonstrated by our ZICs indicates that this class of hybrid devices effectively combines the desirable attributes of electrochemical capacitors, such as the long cycle life and high-power densities, with energy densities approaching those of batteries. This combination is very attractive as power sources for autonomous electronics and Internet-of-Things applications because a long cycle life is crucially needed to lower maintenance costs by avoiding the need for frequent battery replacement. The long cycle lifetime is particularly advantageous when considering large-scale networks consisting of millions of sensors, where the maintenance burden could quickly become unsustainable if frequent battery replacements were required.

In summary, this work demonstrated an easy approach to significantly improve the cycle lifetime and energy density of ZICs by using an electrolyte that facilitated CuZn alloy deposition to suppress dendrites during redox cycling. The characterization of grain orientations and overpotentials during the growth plateau phase revealed the reduced energy barrier for planar growth under the Zn-Cu electrolyte, clarifying the fundamental origins of the enhanced cell stability. ZICs with an n/p ratio of 3.10 showed a high energy density of 41 Wh/kg and capable of enduring 6700 GCD cycles, equivalent to 347 hours before the capacity dropped below 90%. The cumulative capacities of ZICs surpassed previous benchmarks including those of lithium and sodium ion capacitors. The Zn-Cu electrolyte in this study is very promising for implementing robust ZICs for high-performance, low-maintenance electrochemical energy supplies.

METHODS

Preparation of electrolytes

For the Zn-Cu electrolyte, 0.5 M of zinc trifluoromethanesulfonate [$Zn(OTf)_2$, Sigma-Aldrich, 98%] and 0.1 or 0.2 M of copper trifluoromethanesulfonate [$Cu(OTf)_2$, Sigma-Aldrich, 98%] were dissolved in acetonitrile (ACN, Thermo Fisher Scientific, 99.9%) solvent at room temperature. For the Zn-only electrolyte, it was 0.5 M of $Zn(OTf)_2$ dissolved in ACN.

Fabrication of ZICs

For the anode, zinc was deposited on a graphite sheet with electroplating method under 12.5 mA/cm^2 for 10 min. A 0.5 M of zinc triflate electrolyte was used for electroplating solution, and the deposited zinc film was roughly 5 µm thick. The Zn/Zn symmetric cell was fabricated using a CR2032 coin cell package. A pristine Zn foil (10-µm thickness with a diameter of 1.3 cm) and the electroplated zinc electrode were used for cathode and anode, respectively. For the zinc-ion capacitors, the cathodes were activated carbon (Calgon Carbon, YP-50F), conductive carbon black (MTI Corporation), and polyvinylidene fluoride (Solvay PVDF 5130) mixed at a ratio of 8:1:1. The mixture was suspended in 1-methyl-2-pyrrolidinone (Thermo Fisher Scientific, >99.5%) to make a solution of 16.7% solids by weight. The solution was deposited over an area of 1.33 cm^2 on

the carbon cloth (AvCarb, 1071 HCB) with a loading of 10.5 to 25.5 mg/cm^2. The electrode was annealed at 100°C. The anode and cathode were separated by a glass microfiber separator (Cytiva, Whatman GF/A). After adding 160 μl of the electrolyte, the sandwich structure was encapsulated in coin cells (CR2032) by a hydraulic crimping machine (MTI Corporation, MSK-110). The specific details for the cells used in each figure are listed in Table 2. Each measurement was done at least three times and on four samples.

Material and electrochemical characterizations

The morphology change was measured by SEM (FEI Apreo) at 20 kV. The arithmetic mean height was measured by 3D optical profiler (Filmetrics Profilm 3D). The x-ray diffraction patterns were recorded by Rigaku Miniflex XRD at Cu. The measurements of Zn/Zn symmetric cells were conducted by using a galvanostat (Neware) based on two electrode configurations with a cutoff capacity of 0.42 and 0.84 mAh/cm^2 at a current density of 25 mA/cm^2. Other electrochemical measurements were conducted by a potentiostat (SP-200, Bio-Logic). Cyclic voltammetry was scanned between 0 and 2 V with the voltage scan rate range of 1 to 70 mV/s. GCD was conducted under constant current densities in the range of 7.5 to 52.5 mA/cm^2. Electrochemical impedance spectroscopy was performed in the frequency range of 0.1 Hz to 200 kHz at 0 V. Cycling stability measurements were conducted by Neware battery tester.

The energy density E was calculated from GCD characteristics based on the equation of $E = (\int VIdt)/A$ or $E = (\int VIdt)/m$, where A is the electrode area, m is the loading of cathode and anode, V is the potential, and I is the applied current. The power density P was calculated with the equation of $P = E/t$, where t is the discharging time. The capacitance was calculated by $C = \frac{1}{\Delta V \nu}\int_{V_1}^{V_2} i\ dV$. Here V_1 and V_2 are the starting and ending potentials in the discharge portion of the measurement, i is the current at each potential, $\Delta V = V_2 - V_1$ is the potential window, and ν is the voltage scan rate.

The n/p ratio was calculated through dividing the capacity of the zinc anode by the discharge capacity of the cathode. The capacity of the zinc anode was calculated by multiplying the measured weight of the electrodeposited zinc with the theoretical gravimetric capacity of zinc: $Capacity_{\text{anode}} = \frac{820\ \text{mAh/g} \times w_{\text{anode}}}{A}$, where w_{anode} is the anode Zn loading, and A is the area of the anode. The discharge capacity of the cathode was extracted using the equation $Capacity_{\text{cathode}} = \frac{I \times t_d}{A}$, where t_d is the discharging time at a current density of 25 mA/cm^2, and A is the area of the cathode.

The cumulative capacity was calculated from the summation of discharge capacity ($\sum_1^n$ *discharge capacity*) for the number of cycles for which the Coulombic efficiency was over 99%, and the capacity retention exceeded 90%. The GCD data are included in fig. S6.

Supplementary Materials

This PDF file includes:

Notes S1 to S3
Figs. S1 to S6

REFERENCES AND NOTES

1. N. Ogihara, M. Hasegawa, H. Kumagai, R. Mikita, N. Nagasako, Heterogeneous intercalated metal-organic framework active materials for fast-charging non-aqueous Li-ion capacitors. *Nat. Commun.* **14**, 1472 (2023).
2. H. Wang, C. Zhu, D. Chao, Q. Yan, H. J. Fan, Nonaqueous hybrid lithium-ion and sodium-ion capacitors. *Adv. Mater.* **29**, 1702093 (2017).
3. H. S. Hirsh, Y. Li, D. H. S. Tan, M. Zhang, E. Zhao, Y. S. Meng, Sodium-ion batteries paving the way for grid energy storage. *Adv. Energy Mater.* **10**, 2001274 (2020).
4. Y. Zhang, J. Jiang, Y. An, L. Wu, H. Dou, J. Zhang, Y. Zhang, S. Wu, M. Dong, X. Zhang, Z. Guo, Sodium-ion capacitors: Materials, mechanism, and challenges. *ChemSusChem* **13**, 2522–2539 (2020).
5. Time for lithium-ion alternatives. *Nat. Energy* **7**, 461 (2022).
6. J. Yin, W. Zhang, N. A. Alhebshi, N. Salah, H. N. Alshareef, Electrochemical zinc ion capacitors: Fundamentals, materials, and systems. *Adv. Energy Mater.* **11**, 2100201 (2021).
7. L. Wang, M. Peng, J. Chen, T. Hu, K. Yuan, Y. Chen, Eliminating the micropore confinement effect of carbonaceous electrodes for promoting Zn-ion storage capability. *Adv. Mater.* **34**, e2203744 (2022).
8. Z. Xu, R. Ma, X. Wang, Ultrafast, long-life, high-loading, and wide-temperature zinc ion supercapacitors. *Energy Stor. Mater.* **46**, 233–242 (2022).
9. G. Zampardi, F. La Mantia, Open challenges and good experimental practices in the research field of aqueous Zn-ion batteries. *Nat. Commun.* **13**, 687 (2022).
10. M. Kwon, J. Lee, S. Ko, G. Lim, S. H. Yu, J. Hong, M. Lee, Stimulating Cu-Zn alloying for compact Zn metal growth towards high energy aqueous batteries and hybrid supercapacitors. *Energ. Environ. Sci.* **15**, 2889–2899 (2022).
11. L. Ma, M. A. Schroeder, O. Borodin, T. P. Pollard, M. S. Ding, C. Wang, K. Xu, Realizing high zinc reversibility in rechargeable batteries. *Nat. Energy* **5**, 743–749 (2020).
12. L. E. Blanc, D. Kundu, L. F. Nazar, Scientific challenges for the implementation of Zn-ion batteries. *Joule* **4**, 771–799 (2020).
13. Z. Hou, T. Zhang, X. Liu, Z. Xu, J. Liu, W. Zhou, Y. Qian, H. Jin Fan, D. Chao, D. Zhao, A solid-to-solid metallic conversion electrochemistry toward 91% zinc utilization for sustainable aqueous batteries. *Sci. Adv.* **8**, eabp8960 (2022).
14. Y. Yan, C. Shu, T. Zeng, X. Wen, S. Liu, D. Deng, Y. Zeng, Surface-preferred crystal plane growth enabled by underpotential deposited monolayer toward dendrite-free zinc anode. *ACS Nano* **16**, 9150–9162 (2022).
15. Y. Sasaki, K. Yoshida, T. Kawasaki, A. Kuwabara, Y. Ukyo, Y. Ikuhara, In situ electron microscopy analysis of electrochemical Zn deposition onto an electrode. *J. Power Sources* **481**, 228831 (2021).
16. S. J. Banik, R. Akolkar, Suppressing dendrite growth during zinc electrodeposition by PEG-200 additive. *J. Electrochem. Soc.* **160**, D519–D523 (2013).
17. Q. Zhang, J. Luan, L. Fu, S. Wu, Y. Tang, X. Ji, H. Wang, The three-dimensional dendrite-free zinc anode on a copper mesh with a zinc-oriented polyacrylamide electrolyte additive. *Angew. Chem. Int. Ed. Engl.* **58**, 15841–15847 (2019).
18. X. Guo, Z. Zhang, J. Li, N. Luo, G. L. Chai, T. S. Miller, F. Lai, P. Shearing, D. J. L. Brett, D. Han, Z. Weng, G. He, I. P. Parkin, Alleviation of dendrite formation on zinc anodes via electrolyte additives. *ACS Energ. Lett.* **6**, 395–403 (2021).
19. H. Huang, J. Yun, H. Feng, T. Tian, J. Xu, D. Li, X. Xia, Z. Yang, W. Zhang, Towards high-performance zinc anode for zinc ion hybrid capacitor: Concurrently tailoring hydrodynamic stability, zinc deposition and solvation structure via electrolyte additive. *Energy Stor. Mater.* **55**, 857–866 (2023).
20. F. Wang, O. Borodin, T. Gao, X. Fan, W. Sun, F. Han, A. Faraone, J. A. Dura, K. Xu, C. Wang, Highly reversible zinc metal anode for aqueous batteries. *Nat. Mater.* **17**, 543–549 (2018).
21. Y. Wang, R. Zhao, M. Liu, J. Yang, A. Zhang, J. Yue, C. Wu, Y. Bai, Suppressed water reactivity by zincophilic-hydrophobic electrolyte additive for superior aqueous Zn metal batteries. *Adv. Energy Mater.* **13**, 2302707 (2023).
22. Y. Tang, C. Liu, H. Zhu, X. Xie, J. Gao, C. Deng, M. Han, S. Liang, J. Zhou, Ion-confinement effect enabled by gel electrolyte for highly reversible dendrite-free zinc metal anode. *Energy Stor. Mater.* **27**, 109–116 (2020).
23. G. Li, Z. Liu, Q. Huang, Y. Gao, M. Regula, D. Wang, L. Q. Chen, D. Wang, Stable metal battery anodes enabled by polyethylenimine sponge hosts by way of electrokinetic effects. *Nat. Energy* **3**, 1076–1083 (2018).
24. Q. Yang, Y. Guo, B. Yan, C. Wang, Z. Liu, Z. Huang, Y. Wang, Y. Li, H. Li, L. Song, J. Fan, C. Zhi, Hydrogen-substituted graphdiyne ion tunnels directing concentration redistribution for commercial-grade dendrite-free zinc anodes. *Adv. Mater.* **32**, e2001755 (2020).
25. J. Zhi, S. Zhao, M. Zhou, R. Wang, F. Huang, A zinc-conducting chalcogenide electrolyte. *Sci. Adv.* **9**, eade2217 (2023).
26. Z. Wang, J. Huang, Z. Guo, X. Dong, Y. Liu, Y. Wang, Y. Xia, A metal-organic framework host for highly reversible dendrite-free zinc metal anodes. *Joule* **3**, 1289–1300 (2019).
27. P. Chen, X. Sun, T. Pietsch, B. Plietker, E. Brunner, M. Ruck, Electrolyte for high-energy- and power-density zinc batteries and ion capacitors. *Adv. Mater.* **35**, e2207131 (2023).
28. S. B. Wang, Q. Ran, R. Q. Yao, H. Shi, Z. Wen, M. Zhao, X. Y. Lang, Q. Jiang, Lamella-nanostructured eutectic zinc–aluminum alloys as reversible and dendrite-free anodes for aqueous rechargeable batteries. *Nat. Commun.* **11**, 1634 (2020).
29. S. Li, J. Fu, G. Miao, S. Wang, W. Zhao, Z. Wu, Y. Zhang, X. Yang, Toward planar and dendrite-free Zn electrodepositions by regulating Sn-crystal textured surface. *Adv. Mater.* **33**, e2008424 (2021).

30. W. Yuan, X. Nie, G. Ma, M. Liu, Y. Wang, S. Shen, N. Zhang, Realizing textured zinc metal anodes through regulating electrodeposition current for aqueous zinc batteries. *Angew. Chem. Int. Ed. Engl.* **62**, e202218386 (2023).
31. B. Li, K. Yang, J. Ma, P. Shi, L. Chen, C. Chen, X. Hong, X. Cheng, M. C. Tang, Y. B. He, F. Kang, Multicomponent copper-zinc alloy layer enabling ultra-stable zinc metal anode of aqueous Zn-ion battery. *Angew. Chem. Int. Ed. Engl.* **61**, e202212587 (2022).
32. B. Raza, A. Naveed, J. H. Chen, H. C. Lu, T. Rasheed, J. Yang, Y. N. NuLi, J. L. Wang, Zn anode sustaining high rate and high loading in organic electrolyte for rechargeable batteries. *Energy Stor. Mater.* **46**, 523–534 (2022).
33. W. Y. Kim, H. I. Kim, K. M. Lee, E. Shin, X. Liu, H. Moon, H. Adenusi, S. Passerini, S. K. Kwak, S. Y. Lee, Demixing the miscible liquids: Toward biphasic battery electrolytes based on the kosmotropic effect. *Energ. Environ. Sci.* **15**, 5217–5228 (2022).
34. V. Augustyn, P. Simon, B. Dunn, Pseudocapacitive oxide materials for high-rate electrochemical energy storage. *Energ. Environ. Sci.* **7**, 1597–1614 (2014).
35. C. Shin, L. Yao, H. Lin, P. Liu, T. N. Ng, Photothermal supercapacitors with gel polymer electrolytes for wide temperature range operation. *ACS Energy Lett.* **8**, 1911–1918 (2023).
36. L. Yao, K. Zheng, N. Koripally, N. Eedugurala, J. D. Azoulay, X. Zhang, T. N. Ng, Structural pseudocapacitors with reinforced interfaces to increase multifunctional efficiency. *Sci. Adv.* **9**, eadh0069 (2023).
37. L. Yao, J. Liu, N. Eedugurala, P. Mahalingavelar, D. J. Adams, K. Wang, K. S. Mayer, J. D. Azoulay, T. N. Ng, Ultrafast high-energy micro-supercapacitors based on open-shell polymer-graphene composites. *Cell Rep. Phys. Sci.* **3**, 100792 (2022).
38. A. Pei, G. Zheng, F. Shi, Y. Li, Y. Cui, Nanoscale nucleation and growth of electrodeposited lithium metal. *Nano Lett.* **17**, 1132–1139 (2017).
39. K. Yan, J. Wang, S. Zhao, D. Zhou, B. Sun, Y. Cui, G. Wang, Temperature-dependent nucleation and growth of dendrite-free lithium metal anodes. *Angew. Chem. Int. Ed. Engl.* **58**, 11364–11368 (2019).
40. J. Yang, R. Zhao, Y. Wang, Z. Hu, Y. Wang, A. Zhang, C. Wu, Y. Bai, Insights on artificial interphases of Zn and electrolyte: Protection mechanisms, constructing techniques, applicability, and prospective. *Adv. Funct. Mater.* **33**, 2213510 (2023).
41. R. Zhao, J. Yang, X. Han, Y. Wang, Q. Ni, Z. Hu, C. Wu, Y. Bai, Stabilizing Zn metal anodes via Cation/Anion regulation toward high energy density Zn-ion batteries. *Adv. Energy Mater.* **13**, 2203542 (2023).
42. X. Liu, K. Oikawa, Assessment of the temperature and pressure dependence of molar volume and phase diagrams of Cu and Zn. *CALPHAD* **47**, 114–122 (2014).
43. K. Wang, L. Yao, M. Jahon, J. Liu, M. Gonzalez, P. Liu, V. Leung, X. Zhang, T. N. Ng, Ion-exchange separators suppressing self-discharge in polymeric supercapacitors. *ACS Energy Lett.* **5**, 3276–3284 (2020).
44. P. Zou, R. Lin, T. P. Pollard, L. Yao, E. Hu, R. Zhang, Y. He, C. Wang, W. C. West, L. Ma, O. Borodin, K. Xu, X. Q. Yang, H. L. Xin, Localized hydrophobicity in aqueous zinc electrolytes improves zinc metal reversibility. *Nano Lett.* **22**, 7535–7544 (2022).
45. Z. Xu, Y. Li, G. Li, H. Zhang, X. Wang, Reversible zinc powder anode via crystal facet engineering. *Matter* **6**, 3075–3086 (2023).
46. W. Zhang, Y. Dai, R. Chen, Z. Xu, J. Li, W. Zong, H. Li, Z. Li, Z. Zhang, J. Zhu, F. Guo, X. Gao, Z. Du, J. Chen, T. Wang, G. He, I. P. Parkin, Highly reversible zinc metal anode in a dilute aqueous electrolyte enabled by a pH buffer additive. *Angew. Chem. Int. Ed. Engl.* **62**, e202212695 (2023).
47. L. Li, D. Zhang, Y. Gou, J. Fang, Q. Kang, R. Feng, Z. Liang, J. Deng, Lithium/sodium-ion capacitors based on 3D graphene-based materials. *J. Energy Storage* **40**, 102822 (2021).
48. R. Thangavel, B. K. Ganesan, V. Thangavel, W. S. Yoon, Y. S. Lee, Emerging materials for sodium-ion hybrid capacitors: A brief review. *ACS Appl. Energy Mater.* **4**, 13376–13394 (2021).

Acknowledgments: This work used the San Diego Nanotechnology Infrastructure of UCSD. **Funding:** The authors C.S., L.Y., and T.N.N. are grateful for the support from National Science Foundation MCA-2120701 and PFI-2120103. The author S.-Y.J. was supported by the National Research Foundation of Korea 2021R1C1C2009461. **Author contributions:** C.S., L.Y., S.-Y.J., and T.N.N. designed the experiments and analyzed the data. C.S. conducted the fabrication and measurement of the devices. T.N.N. supervised the project. All authors contributed to discussions and writing of the manuscript. **Competing interests:** The authors declare that they have no competing interests. **Data and materials availability:** All data needed to evaluate the conclusions in this paper are present in the paper and/or the Supplementary Materials.

Submitted 20 September 2023
Accepted 28 November 2023
Published 3 January 2024
10.1126/sciadv.adf9951

Science Advances

Zinc-copper dual-ion electrolytes to suppress dendritic growth and increase anode utilization in zinc ion capacitors

Chanho Shin, Lulu Yao, Seong-Yong Jeong, and Tse Nga Ng

Sci. Adv. **10** (1), eadf9951. DOI: 10.1126/sciadv.adf9951